Journal of Solid State Chemistry **166,** 400–414 (2002)
doi:10.1006/jssc.2002.9614

X-Ray Structural Determination of a Multilayered Magnetic Dielectric Ceramic $Ba_{42}Ti_{51}Fe_{20}O_{174}$ in the $BaO–TiO_2–Fe_2O_3$ System

V. M. Nassif,* R. E. Carbonio,* J. L. Hodeau,†,[1] and E. Dooryhée†

*INFIQC, Departamento de Físicoquímica, Facultad de Ciencias Químicas, Universidad Nacional de Córdoba, Ciudad Universitaria, 5000 Córdoba, Argentina; and †Laboratoire de Cristallographie CNRS, BP 166X, 38042 Grenoble Cedex, France

Received November 1, 2001; in revised form February 15, 2002; accepted March 1, 2002

Crystallographic studies and refinement of a *native multilayered* phase ($Ba_{42}Ti_{51}Fe_{20}O_{174}$), occurring in the $BaO–TiO_2–Fe_2O_3$ system for a Ba:Ti:Fe composition close to 2:2:1, were undertaken using synchrotron X-ray powder diffraction. In this area of the $BaO-TiO_2-Fe_2O_3$ phase diagram, numerous ternary compounds were found for extremely close chemical and thermal conditions and multilayered phases were always prepared together with a few adjacent phases. The structure of the multilayered compound ($Ba_{42}Ti_{51}Fe_{20}O_{174}$: space group $C2/m$, $a = 9.9512(2)$ Å, $b = 17.2366(4)$ Å, $c = 42.5272(2)$ Å, $\alpha = 90°$, $\beta = 94.4949(5)°$, $\gamma = 90°$, $V = 7272.04$ Å^3, $\rho = 5.62$ g/cm^3, $Z = 2$) has been solved by Rietveld analysis of a multiphase pattern containing two other known phases ($Ba_{12}Ti_{15}Fe_{28}O_{84}$: space group $C2/m$, $a = 9.9792(2)$ Å, $b = 17.2883(6)$ Å, $c = 19.1714(4)$ Å, $\alpha = 90°$, $\beta = 99.7253(6)°$, $\gamma = 90°$, $V = 3260.04$ Å^3, $\rho = 5.30$ g/cm^3, $Z = 2$, and c-$Ba_{0.925}Fe_{0.075}O_3$: space group $Pm\bar{3}m$, $a = 4.00779(1)$ Å, $\alpha = \beta = \gamma = 90°$, $V = 64.38$ Å^3, $\rho = 6.04$ g/cm^3, $Z = 1$). This multilayered structure adopts a 54-layer close-packed structure built with a $(chcchhhhcchhhhcchc)_3$ (Ba,O) stacking along the *c*-axis to give rise to a very long ($c_{rh} = 127.19$ Å) rhombohedral *c*-axis. Octahedral sites are occupied by a mixture of Ti^{4+} and Fe^{3+} cations and tetrahedral ones by Fe^{3+} cations. © 2002 Elsevier Science (USA)

Key Words: **multilayered ceramic; synchrotron radiation powder diffraction; barium–iron–titanium series; $Ba_{42}Ti_{51}Fe_{20}O_{174}$ crystal structure.**

INTRODUCTION

Magnetic dielectric ceramics are of interest as circulators and isolators for several electronic applications in communication systems (1). Properties such as high dielectric constant, low dielectric loss and high saturation magnetization are required. On the one hand, barium polytitanates are used in many dielectric applications, where improved materials with higher dielectric properties are looked for to enhance miniaturization. On the other hand, materials in current use for magnetic properties include garnets, spinels and the hexaferrite family $BaFe_{12}O_{19}$ (2). For these reasons, it is of interest to study the $BaO–TiO_2–Fe_2O_3$ system to combine the dielectric properties of barium titanates with the magnetic properties of iron oxides. Vanderah *et al.* (3) have studied the phase diagram of this system. It is quite complex and gives rise to at least 16 ternary compounds, most of them having new structures. Some of them, labeled E, J, K, L, M and N in this previous phase diagram study, are particularly interesting, since they correspond to an intermediate composition between the dielectric $BaTiO_3$ and the magnetic $BaFe_{12}O_{19}$. Electron diffraction and high-resolution microscopy investigations of these compounds for a Ba:Ti:Fe ratio close to 2:2:1 suggest that some of these phases present structures with an ordered intergrowth of the hexagonal h-$BaTiO_3$ structure with another structure related to those of $Ba_{12}Ti_{15}Fe_{28}O_{84}$ compound (4). As both $Ba_{12}Ti_{15}Fe_{28}O_{84}$ (5) and hexagonal h-$Ba(Ti,Fe)O_3$ (6) structures are based on a framework of close-packed (cp) (Ba,O) or oxygen layers, where Fe^{3+} and Ti^{4+} cations fill most of the octahedral sites and a few tetrahedral sites, several ternary Ba–Ti–Fe–O structures presenting different cp stacking are possible. Bendersky and Bonevich (7) suggested that at least six of these compounds could present the stacking of titanium-rich and/or iron-rich slabs, which generates "self-assembled" magnetic multilayers with crystallographically flat interfaces. For indexing the most intense reflections, they proposed unit cells with nearly the same hexagonal basal parameters ($a_{hex} = 5.75$ Å) and different *c* parameters (E: 10 cp-layers $c_{hex} \cong 23.7$ Å, K and M: 26 cp-layers $c_{hex} \cong 61.5$ Å, N: 48 cp-layers $c_{rh} \cong 112.7$ Å, J: 54 cp-layers $c_{rh} \cong 127.19$ Å and L: 72 cp-layers $c_{rh} \cong 169.14$ Å) corresponding to different cp stacking of (Ba,O) planes. However, models of these possible "multilayered phases"

[1] To whom correspondence should be addressed. Fax: +33-476881038. E-mail: hodeau@polycnrs-gre.fr.

0022-4596/02 $35.00

are only based on electron diffraction and microscopy data and on the cell-parameter characteristics. Complete structural studies based on X-ray-diffracted intensities are therefore required.

For a Ba:Ti:Fe ratio close to 2:2:1, the complexity of the $BaO:TiO_2:Fe_2O_3$ phase diagram is such that it is a challenge to obtain single crystals of "multilayered phases". An extended range of Ba–Ti–Fe–O phases are crystallized and "multilayered" crystals must intrinsically contain stacking faults which restrict the possibilities in structure determinations (8). Our goal in this contribution is to perform the Rietveld simulations and/or refinements of the X-ray diffraction patterns of such multiphase powdered materials, in order to extract their (Ba,O) cp stacking sequence and the Ti/Fe location in the intermediate planes. However, powder samples of this complex ternary system are generally multiphases composed of "multilayered phases" with large stacking c cell parameters. Thus, to decrease reflection overlaps, Rietveld analysis has been based on high-resolution synchrotron radiation powder diffraction data. The complexity of the powder pattern and the number of structural variables is such that we have constrained some structural parameters to those found in closely related known structures, at least for the known additional phases present in the preparation. We present herein the structure of the so-called "J-phase" with a rhombohedral close packing of 3×18 slabs generating a very long c_{rh} axis ($c_{rh} = 127.19$ Å).

EXPERIMENTAL METHODS

The polycrystalline samples used for the data analysis were prepared using a precipitation method, starting from solutions of $Ba(NO_3)_2$, $Fe(NO_3)_3$, and liquid $TiCl_4$, in stoichiometric ratio to obtain "$Ba_{42}Ti_{49}Fe_{28}O_{182}$." NH_3 was added so as to obtain pH = 10, then the precipitate was filtered and dried. This method, different from those reported by Vanderah *et al.* (3), allowed us to reduce the time of the thermal treatment. The sample was first calcined at 800°C for 12 h, then repetitive annealings (5 days at 1270°C each) were required to reach the final phases J, L, c-$BaTiO_3$, h-Ba(Ti,Fe)O_3, $Ba_{12}Ti_{15}Fe_{28}O_{84}$ (here labeled as the Grey phase). At each step, laboratory X-ray powder patterns were collected to identify the different phases. Our electron diffraction and microscopy analyses on synthesized powders showed layered phases presenting long c axes and cell parameters close to those reported by Bendersky *et al.* (9).

The "multilayered" phases are located in the minimum melting region of the $BaO:TiO_2:Fe_2O_3$ phase diagram and seem to melt incongruently (3). In this area, the stability region of a given phase is extremely narrow and it is extremely difficult to determine the composition and temperature conditions required for preparing a single phase. Furthermore, the lattice parameters of the possible "multilayered" phases E, J, K, L, M and N are very large and closely related to one another. This gives rise to an important overlapping of the individual X-ray diffraction patterns. The determination of the compound stoichiometry by the disappearing phase method was performed, first by using good-resolution X-ray patterns taken with a laboratory equipment associated with an analyzer detection, and then by using high-resolution powder synchrotron radiation patterns taken at the BM16 beam line at the ESRF (10) with a multianalyzer detection system, which allows a reflection width smaller than 0.006° in 2Θ (11). Nevertheless, it was quite impossible to obtain in a reasonable time a pure single multilayered phase. For this reason, X-ray pattern simulations and refinements were performed on multiphased powder patterns presenting one multilayered phase associated with several structurally known phases.

As an example, for the preparation with the nominal composition "$Ba_{42}Ti_{49}Fe_{28}O_{182}$," we synthesized phases J, L, $Ba_{12}Ti_{15}Fe_{28}O_{84}$, cubic c-Ba(Ti,Fe)$O_3$ and hexagonal h-Ba(Ti,Fe)O_3. Since these multilayered structures correspond to different cp stackings of (Ba,O) or (O) layers along the large c-axis, stacking faults could be present along this axis as already shown by previous electron microscopy (TEM) studies (9) and on our TEM observations. As reported by Bendersky *et al.* (9), such stacking faults could induce two types of structural disorder. The first type of disorder corresponds to a positional disorder of pseudo-"$Ba_{12}Ti_{15}Fe_{28}O_{84}$" structural blocks, their structure remaining uniform within each slab. This type of disorder induces some diffuse intensity on weak reflections corresponding to the triple b-axis related to the cell of the "$Ba_{12}Ti_{15}Fe_{28}O_{84}$" structural block. Such superstructure reflections can be spread out on highly disordered crystallites; thus, the remaining stronger reflections give rise to the smallest cell reported by Vanderah *et al.* (3). In our refinement procedure, we use the large monoclinic cells proposed by Bendersky *et al.* (9) since they contain the intrinsic lower symmetry of these blocks. The second type of disorder corresponds to different thicknesses of the "h-$BaTiO_3$" structural blocks, giving rise to the different E, J, K, L, M and N structures. In this case, the presence of several very long c-axis phases such as intergrowth phases corresponding to regular stacking faults along the c-axis could also be expected. However, in the high-resolution powder patterns collected on our samples, reflections are quite sharp and we can perform accurate lattice parameter refinements in the $C2/m$ space group for both, J and L phases. As example, in the "$Ba_{42}Ti_{49}Fe_{28}O_{182}$" preparation, the refinement gives for phase J: $a = 9.9528(2)$ Å, $b = 17.2384(4)$ Å, $c = 42.5216(2)$ Å, $\alpha = 90°$, $\beta = 94.494(2)°$, $\gamma = 90°$; and for phase L: $a = 9.9449(4)$ Å, $b = 17.2262(6)$ Å,

$c = 56.4762(10)$ Å, $\alpha = 90°$, $\beta = 93.320(3)°$, $\gamma = 90°$. The small values of the fitting standard deviation do not take into account the uncertainties on wavelength and temperature values. Nevertheless, the relative difference between the refined lattice parameters of the respective J and L phases is significant since the experimental sources of error are the same on a single diagram. These different a and b parameters are incompatible with a single phase with an intermediate and longer cp order along the c-axis. The J and L phases present very long rhombohedral c_{rh} parameters (J: $c_{rh} = 127.17$ Å, L: $c_{rh} = 169.14$ Å) and all powder patterns containing both phases exhibit a tremendous overlapping even with the high 2Θ experimental resolution of BM16 and the good sample crystallinity (FWHM = 0.020–0.025° in 2Θ). As both J and L phases are unknown, the crystal structure solving was impossible.

Nevertheless, these high-resolution patterns were essential to determine precisely the cell parameters and to identify the reflections of the different constituent phases. Finally, we chose a nominal composition giving rise to the J-phase only, associated with the known phases having smaller cell parameters. Fig. 1 presents one of the X-ray pattern regions easily usable to identify the presence of different phases. It corresponds to a 2Θ range where intense reflections of each phase do not overlap. This pattern was prepared by using the same precipitation method, with a slightly different stoichiometry, and corresponds to a nominal composition "$Ba_{42}Ti_{47.6}Fe_{28}O_{179.2}$." The sample was first calcined at 800°C for 12 h and annealed in air at 1260-1270°C for 32 h. Such a pattern contains the J-phase (space group $C2/m$, $a = 9.9512(2)$ Å, $b = 17.2366(4)$ Å, $c = 42.5272(2)$ Å, $\alpha = 90°$, $\beta = 94.4949(5)°$, $\gamma = 90°$, $V = 7272.03$ Å^3, $\rho = 5.62$ g/cm^3, $Z = 2$) and two other known phases (Grey : $Ba_{12}Ti_{15}Fe_{28}O_{84}$, space group $C2/m$, $a = 9.9792(2)$ Å, $b = 17.2883(6)$ Å, $c = 19.1714(4)$ Å, $\alpha = 90°$, $\beta = 99.7253(6)°$, $\gamma = 90°$, $V = 3260.04$ Å^3, $\rho = 5.30$ g/cm^3, $Z = 2$; C: c-Ba(Ti,Fe)O_3, space group $Pm\bar{3}m$, $a = 4.00779(1)$ Å, $\alpha = \beta = \gamma = 90°$, $V = 64.38$ Å^3, $\rho = 6.04$ g/cm^3, $Z = 1$). The Miller indices of the weak reflections occurring at very low Bragg angles are reported in the insert of Fig. 1 and justify the large monoclinic cell used for the refinement. Superstructure reflections corresponding to the triple b-axis are very weak on the X-ray patterns. Due to the richness of the phase diagram and the relatively small equilibrium time used for the heat treatment, we cannot exclude the presence of stacking faults in phase J giving rise to the two types of disorder presented previously. Nevertheless, the reflection peaks for the J-phase are surprisingly sharper (0.020° in 2Θ) than those of the Grey phase. Thus, for the simulations/refinements, we have first considered the J-phase as an ordered phase.

For intensity analysis, a full powder pattern was collected at room temperature at the BM2-D2AM beam line at the European Synchrotron Radiation Facility using the Debye–Scherrer geometry. The sample was contained in a glass capillary (0.7 mm diameter) which was rotated during data collection for a better sampling. The X-ray

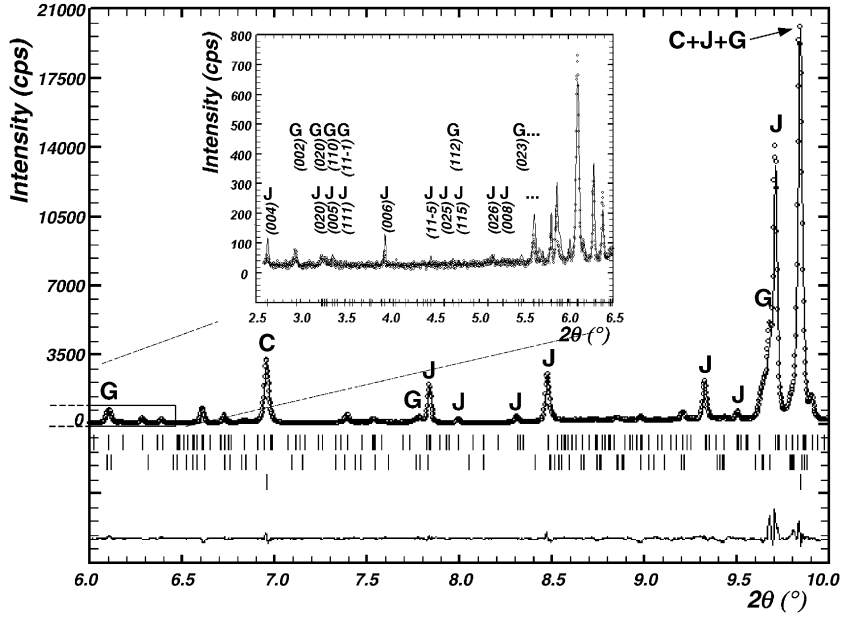

FIG. 1. Enlargement of the low 2Θ area (2Θ < 10°) of the synchrotron X-ray powder pattern where we can separate strong reflections of the J, Grey and C phases. Observed (dots), calculated (line), difference (bottom) and Bragg reflections (|) are represented on this pattern collected at the D2AM-ESRF facility (refinement A). The insert enlarges the very low 2Θ area (2.5–6.5°) and reports Miller indices of all the weak reflections occurring at very low Bragg angle, justifying the large cell used for the refinement. $\lambda = 0.48631(5)$Å.

wavelength, selected by a Si(1 1 1) double monochromator, was $\lambda = 0.48632(5)$ Å associated with a 95% σ-polarization rate. The sample absorption coefficient was ($\mu = 59.53\,cm^{-1}$). After Lorentz, polarization and absorption corrections, the structure factors were calculated using the scattering factors of Cromer and Waber (12), and the anomalous factors f' and f'' calculated by Sasaki (13) using the Cromer and Liberman method (14,15). Structural refinements and simulations were carried out with the Rietveld (16) method by using the Fulproff program (17). Refinements were based initially on data with $2.5^\circ < 2\theta < 22^\circ$ and finally on data with $6^\circ < 2\theta < 32.8^\circ$ to increase the number of reflections up to 8919.

REFINEMENT PROCEDURE

Due to the large cell parameter of the unknown phase and the presence of coexisting known phases, the number of reflections is enormous and the powder pattern presents a severe reflection overlapping. To reduce the number of variables, the two known phases $Ba_{12}Ti_{15}Fe_{28}O_{84}$ and c-Ba(Ti,Fe)O_3 were introduced with fixed atomic positions corresponding to published structures (5, 18). Only their cell parameters and the peak profile parameters U, V, W, X and Y corresponding to the Thompson–Cox–Hastings pseudo-Voigt convoluted with an axial divergence asymmetry function (19) were initially refined. The corresponding final parameters are reported in Table 1.

For the first simulations of the unknown J-phase, only the hexagonal (Ba,O) stacking was introduced with all different A, B and C possibilities, then the Ba occupancies were refined to determine the respective Ba/O atomic location in this (Ba,O) framework. For these initial simulations, the theoretical atomic positions are derived from $x = m/12 - \delta x$ with $m = 3q$, $3q + 1$ or $3q + 2$ (according to B, A or C possibilities) for a given layer, $y = n/12$ with n odd or even, $z = p/36$ with p odd for O/Ba atoms and even for Ti/Fe atoms. Along the a-axis, the additional δx shift takes into account the β angle of the monoclinic cell and corresponds to $\delta x = p/(3 \times 36)$. Finally, the stacking of the 3×18 (Ba,O) layers gives rise to the rhombohedral cell sketched in Fig. 2. These Ba positions account for the intensities of the most intense reflections. The corresponding oxygen framework generates the octahedral and tetrahedral sites, all of which were initially occupied by Ti/Fe cations. Subsequent occupancy refinements allow the determination of the sites which are really occupied and, thus give the octahedron/tetrahedron stacking along the c-axis. As the correlation between the parameters was huge, to prevent false minima, we have used no pre-determined models for Ti/Fe location, as those of Bendersky *et al.* (9) or Grey *et al.* (5), and several refinements/simulations were initiated using different starting points. Finally, the best agreement was obtained for the (Ba,O) stacking $(chcchhhhcchhhhcchc)_3$ giving rise to a $Ba_{42}O_{174}$ polyhedral stacking related to those proposed by Bendersky *et al.* $(chcchchcccchchcchc)_3$. All atomic xyz coordinates of Ba and Ti/Fe atoms, and the z coordinate of oxygen atoms were independently refined. No significant improvement was obtained when we refined all xyz coordinates of oxygen atoms relative to refinements performed with fixed x and y values and the same z coordinate for all O atoms lying in the same (Ba,O) layer. Thus, we finally used this latter procedure to decrease the number of variables. At this step, tetrahedral sites were assumed to be fully occupied by Fe^{3+} and octahedral sites by Fe^{3+} and/or Ti^{4+}, which have similar ionic radii (20). The sensitivity of our Rietveld refinements to the Ti/Fe occupancy was not significant, so in the last fits reported in Tables 2–5, we used the overall Fe/Ti occupancy factors affected with fixed thermal parameters corresponding to the thermal Debye–Waller parameters refined for the cubic c-Ba(Ti,Fe)O_3 phase. The overall Fe/Ti occupancy was chosen on the basis of the electroneutrality of the J-phase, assuming Ba^{2+}, Fe^{3+}, Ti^{4+} cations and no oxygen vacancies in the (Ba,O) framework. No statistical improvement was obtained in the final agreement factors by assuming different Ti/Fe occupancies and the presence of O vacancies as it could exist in the h-$BaTiO_{3-x}$ phase (6). To uncorrelate the Ti/Fe occupancies, additional experiments on closely related samples with slightly different phases and/or chemically sensitive experiments, such as X-ray anomalous or neutron-scattering measurements, are needed. Consequently, the final refinement (refinement A) was carried out assuming full cationic and anionic site occupancies and the formulae for the J-phase corresponds to $Ba_{42}Ti_{51}Fe_{20}O_{174}$. The weighted profile agreement factor

TABLE 1
Lattice and Profile Parameters Used for the Structural Determination of the J, Grey, and C Phases by Rietveld Analysis of the High-Resolution Powder D2AM-ESRF Data

Phase	a (Å)	b (Å)	c (Å)	β (deg.)	U	V	W	X	Y	LorSiz
J	9.9512(2)	17.2366(4)	42.5272(2)	94.4949(5)	0.00472	−0.00207	0.00048	0.08273	0.00117	—
Grey	9.9792(2)	17.2883(6)	19.1714(4)	99.7253(6)	0.00943	−0.00415	0.00096	0.16554	0.00233	—
C	4.00779(1)	4.00779(1)	4.00779(1)	90.000	0.00926	−0.00172	0.00043	0.12508	0.00121	0.00549

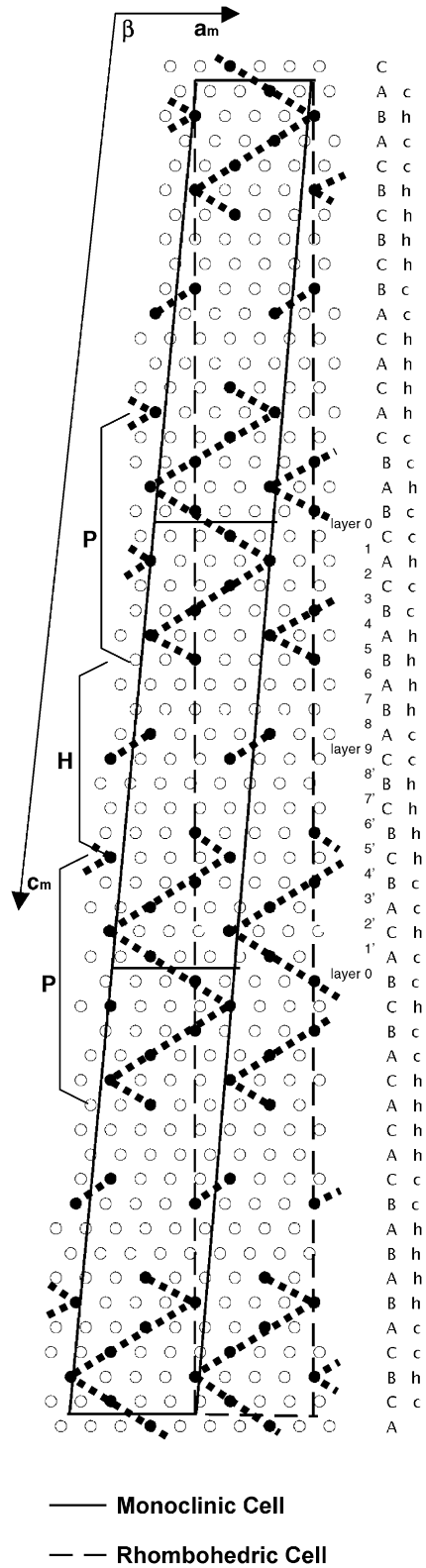

FIG. 2. Stacking of (Ba,O) atoms along the *c*-axis for the J-phase (○: open spheres, Ba:full spheres), the monoclinic and rhombohedric cell are schematized, the $(hcchhhhcchhhhcchc)_3$ sequence and the H and P blocks are outlined.

TABLE 2
Agreement Factors for the Two Rietveld Refinements A and B (See Text)

	Refinement A			Refinement B		
	J-phase	Grey phase	C-phase	J-phase	Grey phase	C-phase
R_p%		10.3			9.98	
R_{wp}%		14.3			13.4	
R_{Bragg}%	6.30	9.97	2.40	6.06	8.02	2.31

was 14.3% corresponding to a 6.30% R_{Bragg} factor for the unknown J-phase, 9.97% for the Grey phase and 2.40% for the c-$Ba(Ti,Fe)O_3$ phase. The respective phase mass fractions were 45.30%, 25.20% and 29.50%, respectively, and corresponded to the overall composition $Ba_{42}Ti_{46.0}Fe_{27.6}O_{176.4}$ close to the initial preparation $Ba_{42}Ti_{47.6}Fe_{28}O_{179.2}$. As said above, to avoid refinement artifacts, for all our calculations we fixed the positional atomic parameters of the two additional phases to values already published (5, 18). Only the Ti/Fe occupancy factor and the atomic and Debye–Waller thermal factors of the cubic phase were refined, since this phase presents a limited number of atomic parameters. The agreement between the observed and calculated intensities and their difference are reported in the full pattern of Fig. 3 and in the corresponding partial patterns. The cell parameters of the three phases and their profile parameters are reported in Table 1, the agreement factors are given in the first column of Table 2. The Ti/Fe occupancy and the atomic positions for both C and Grey phases are reported in the first column of Tables 3–4, the atomic positions for the J-phase are reported in the first column of Table 5.

At this stage, R_{Bragg} for the $Ba_{12}Ti_{15}Fe_{28}O_{84}$ phase was relatively high (9.97%) and it can be seen from the insert of Fig. 3 that the largest disagreement occurs for the strongest peaks of this phase. Its lattice parameters are slightly different than those published in Ref. (5). These differences are significant and mean that our powdered sample is slightly different from the reported single crystal (5), due to the different heat treatment conditions. Thus it is probable that the Fe/Ti contents and the atomic positions of the Grey phase are also slightly different from those reported

TABLE 3
Atomic Coordinates, Occupancy, and Isotropic Thermal Factor for the C-Phase: c-$Ba(Ti,Fe)O_3$ Corresponding to Refinements A (First Column) and B (Second Column)

Atom	Site	*x*	*y*	*z*	Biso	Refinement A Fe occupancy	Refinement B Fe occupancy
Ba	1*a*	0	0	0	0.66(1)		
M: (Ti/Fe)	1*b*	$\frac{1}{2}$	$\frac{1}{2}$	$\frac{1}{2}$	0.61(4)	0.074(14)	0.075(14)
O	3*c*	$\frac{1}{2}$	$\frac{1}{2}$	0	0.87(5)		

TABLE 4
Atomic Coordinates, Occupancy, and Isotropic Thermal Factor for the Grey Phase: $Ba_{12}Ti_{15}Fe_{28}O_{84}$ Corresponding to Initial Data of Ref. (5) (Refinement A, First Column) and Refinement B (Second Column)

		Refinement A				Refinement B			
Atom	Site	*x*	*y*	*z*	Fe occupancy	*x*	*y*	*z*	Fe occupancy
Ba(1)	8*j*	0.3174	0.1633	0.4381		0.317(1)	0.1615(7)	0.4349(5)	
Ba(2)	4*i*	0.8076	0	0.4405		0.811(2)	0	0.4392(7)	
Ba(3)	8*j*	0.4387	0.3327	0.3107		0.442(1)	0.3300(7)	0.3103(4)	
Ba(4)	4	0.3512	0	0.0839		0.368(2)	0	0.0916(7)	
M(1)	2*a*	0	0	0	1.0	0	0	0	1.0
M(2)	8*j*	0.1714	0.1720	0.0272	1.0	0.162(2)	0.166(2)	0.037(1)	1.0
M(3)	4*g*	0	0.3442	0	0.9	0	0.354(2)	0	0.9
M(4)	4*i*	0.7039	0	0.1112	0.83	0.723(4)	0	0.117(1)	0.83
M(5)	8*j*	0.9520	0.2583	0.1327	0.87	0.952(2)	0.258(1)	0.132(1)	0.87
M(6)	8*j*	0.7097	0.1644	0.1332	0.91	0.723(2)	0.171(2)	0.124(1)	0.91
M(7)	8*j*	0.9835	0.0858	0.1335	0.88	0.966(2)	0.091(1)	0.127(1)	0.88
M(8)	4*i*	0.2697	$\frac{1}{2}$	0.2594	0.68	0.275(4)	$\frac{1}{2}$	0.254(2)	0.68
M(9)	8*j*	0.5098	0.0927	0.2502	0.24	0.499(3)	0.088(2)	0.233(1)	0.24
M(10)	4*i*	0.2368	0	0.2519	0.33	0.227(4)	0	0.261(2)	0.33
M(11)	8*j*	0.2396	0.1762	0.2487	0.58	0.247(3)	0.171(2)	0.252(1)	0.58
M(12)	8*j*	0.1370	0.3250	0.3803	0.37	0.126(3)	0.333(2)	0.378(1)	0.37
M(13)	4*i*	0.1132	0	0.3807	0.30	0.103(4)	0	0.390(2)	0.30
M(14)	4*i*	0.4714	0	0.4044	1.0	0.474(3)	0	0.388(1)	1.0
M(15)	4*h*	0	0.1665	$\frac{1}{2}$	0.39	0	0.154(2)	$\frac{1}{2}$	0.39
O(1)	4*i*	0.3054	0	0.4331		0.3054	0	0.4331	
O(2)	8*j*	0.3168	0.3322	0.4373		0.3168	0.3322	0.4373	
O(3)	8*j*	0.0626	0.0830	0.4385		0.0626	0.0830	0.4385	
O(4)	8*j*	0.0658	0.2493	0.4378		0.0658	0.2493	0.4378	
O(5)	8*j*	0.0681	0.4108	0.4322		0.0681	0.4108	0.4322	
O(6)	8*j*	0.4530	0.1683	0.3111		0.4530	0.1683	0.3111	
O(7)	4*i*	0.4342	$\frac{1}{2}$	0.3199		0.4342	$\frac{1}{2}$	0.3199	
O(8)	4*i*	0.4397	0	0.3045		0.4397	0	0.3045	
O(9)	8*j*	0.1832	0.0796	0.3113		0.1832	0.0796	0.3113	
O(10)	8*j*	0.1987	0.2428	0.3191		0.1987	0.2428	0.3191	
O(11)	8*j*	0.1893	0.4126	0.3104		0.1893	0.4126	0.3104	
O(12)	8*j*	0.0620	0.1711	0.1896		0.0620	0.1711	0.1896	
O(13)	8*j*	0.0597	0.3377	0.1824		0.0597	0.3377	0.1824	
O(14)	4*i*	0.0792	0	0.1837		0.0792	0	0.1837	
O(15)	4*i*	0.0777	$\frac{1}{2}$	0.1961		0.0777	$\frac{1}{2}$	0.1961	
O(16)	8*j*	0.3186	0.0857	0.2024		0.3186	0.0857	0.2024	
O(17)	8*j*	0.3092	0.2520	0.1899		0.3092	0.2520	0.1899	
O(18)	8*j*	0.3137	0.4218	0.1839		0.3137	0.4218	0.1839	
O(19)	8*j*	0.3558	0.1675	0.0597		0.3558	0.1675	0.0597	
O(20)	8*j*	0.3641	0.3305	0.0743		0.3641	0.3305	0.0743	
O(21)	4*i*	0.3762	$\frac{1}{2}$	0.0714		0.3762	$\frac{1}{2}$	0.0714	
O(22)	8*j*	0.1009	0.0814	0.0599		0.1009	0.0814	0.0599	
O(23)	8*j*	0.0978	0.2594	0.0659		0.0978	0.2594	0.0659	
O(24)	8*j*	0.1090	0.4175	0.0605		0.1090	0.4175	0.0605	

Note. Biso thermal factors for Ba^{2+}, [Fe^{3+}, Ti^{4+}] and O^{2-} are 0.66(1), 0.61(4) and 0.87(5), respectively.

for the single crystal synthesized by slow-cooling (from 1300°C) with KBO_2 as a flux. Consequently, for subsequent refinements, the *xyz* cationic coordinates of the $Ba_{12}Ti_{15}Fe_{28}O_{84}$ phase were refined together with those of the J-phase (refinement B). For all phases, the thermal factors were fixed identical for all atoms of the same type. No significant changes in atomic positions occur and a slightly better agreement between observed and calculated intensities is obtained for this refinement B. The results are reported in Fig. 4. The final weighted profile agreement factor was 13.40% corresponding to a 6.06% Bragg *R*-factor for the unknown J-phase, 8.02% for the Grey phase

TABLE 5
Atomic Coordinates, Occupancy, and Isotropic Thermal Factor for the J-Phase: $Ba_{42}Ti_{51}Fe_{20}O_{174}$ Corresponding to Refinements A (First Column) and B (Second Column)

		Refinement A				Refinement B			
Atom	Site	x	y	z	Fe occupancy	x	y	z	Fe occupancy
Ba(04)	4*i*	0.317(3)	0	−0.0355(3)		0.313(3)	0	−0.0352(3)	
Ba(06)	8*j*	0.324(2)	0.330(1)	−0.0301(2)		0.327(2)	0.331(1)	−0.0305(2)	
Ba(12)	8*j*	0.474(2)	0.164(1)	−0.0833(2)		0.471(2)	0.166(1)	−0.0833(2)	
Ba(14)	4*i*	0.468(3)	$\frac{1}{2}$	−0.0817(4)		0.470(3)	$\frac{1}{2}$	−0.0824(4)	
Ba(24)	4*i*	0.282(3)	0	−0.1328(4)		0.279(3)	0	−0.1333(4)	
Ba(26)	8*j*	0.291(2)	0.330(1)	−0.1316(2)		0.289(2)	0.329(1)	−0.1314(2)	
Ba(32)	8*j*	0.097(2)	0.164(1)	−0.1925(2)		0.095(2)	0.165(1)	−0.1924(2)	
Ba(34)	4*i*	0.094(3)	$\frac{1}{2}$	−0.1947(4)		0.095(3)	$\frac{1}{2}$	−0.1952(4)	
Ba(12)	8*j*	0.428(2)	0.166(1)	−0.2506(2)		0.420(2)	0.166(1)	−0.2506(2)	
Ba(44)	4*i*	0.401(2)	$\frac{1}{2}$	−0.2485(4)		0.397(2)	$\frac{1}{2}$	−0.2487(4)	
Ba(57)	4*i*	0.042(2)	$\frac{1}{2}$	−0.3146(3)		0.039(2)	$\frac{1}{2}$	−0.3146(3)	
Ba(72)	8*j*	0.026(2)	0.169(1)	−0.4143(2)		0.029(2)	0.169(1)	−0.4142(1)	
Ba(85)	8*j*	0.348(2)	0.165(1)	−0.4712(2)		0.348(2)	0.164(1)	−0.4712(2)	
Ba(87)	4*i*	0.350(3)	$\frac{1}{2}$	−0.4683(4)		0.342(3)	$\frac{1}{2}$	−0.4682(4)	
O(01)	8*j*	0.074	0.083	−0.0290(5)		0.074	0.083	−0.0289(5)	
O(02)	8*j*	0.074	0.250	−0.0290(5)		0.074	0.250	−0.0289(5)	
O(03)	8*j*	0.074	0.417	−0.0290(5)		0.074	0.417	−0.0289(5)	
O(05)	8*j*	0.324	0.167	−0.0290(5)		0.324	0.167	−0.0289(5)	
O(07)	4*i*	0.324	$\frac{1}{2}$	−0.0290(5)		0.324	$\frac{1}{2}$	−0.0289(5)	
O(11)	4*i*	0.472	0	−0.0812(5)		0.472	0	−0.0808(5)	
O(13)	8*j*	0.472	0.333	−0.0812(5)		0.472	0.333	−0.0808(5)	
O(15)	8*j*	0.222	0.083	−0.0812(5)		0.222	0.083	−0.0808(5)	
O(16)	8*j*	0.222	0.250	−0.0812(5)		0.222	0.250	−0.0808(5)	
O(17)	8*j*	0.222	0.417	−0.0812(5)		0.222	0.417	−0.0808(5)	
O(21)	8*j*	0.037	0.083	−0.1407(6)		0.037	0.083	−0.1405(5)	
O(22)	8*j*	0.037	0.250	−0.1407(6)		0.037	0.250	−0.1405(5)	
O(23)	8*j*	0.037	0.417	−0.1407(6)		0.037	0.417	−0.1405(5)	
O(25)	8*j*	0.287	0.167	−0.1407(6)		0.287	0.167	−0.1405(5)	
O(27)	4*i*	0.287	$\frac{1}{2}$	−0.1407(6)		0.287	$\frac{1}{2}$	−0.1405(5)	
O(31)	4*i*	0.102	0	−0.1930(5)		0.102	0	−0.1930(5)	
O(33)	8*j*	0.102	0.333	−0.1930(5)		0.102	0.333	−0.1930(5)	
O(35)	8*j*	0.352	0.083	−0.1930(5)		0.352	0.083	−0.1930(5)	
O(36)	8*j*	0.352	0.250	−0.1930(5)		0.352	0.250	−0.1930(5)	
O(37)	8*j*	0.352	0.417	−0.1930(5)		0.352	0.417	−0.1930(5)	
O(41)	4*i*	0.417	0	−0.2506(5)		0.417	0	−0.2501(5)	
O(43)	8*j*	0.417	0.333	−0.2506(5)		0.417	0.333	−0.2501(5)	
O(45)	8*j*	0.167	0.083	−0.2506(5)		0.167	0.083	−0.2501(5)	
O(46)	8*j*	0.167	0.250	−0.2506(5)		0.167	0.250	−0.2501(5)	
O(47)	8*j*	0.167	0.417	−0.2506(5)		0.167	0.417	−0.2501(5)	
O(51)	8*j*	0.315	0.083	-0.3050(5)		0.315	0.083	−0.3050(5)	
O(52)	8*j*	0.315	0.250	−0.3050(5)		0.315	0.250	−0.3050(5)	
O(53)	8*j*	0.315	0.417	−0.3050(5)		0.315	0.417	−0.3050(5)	
O(54)	4*i*	0.065	0	−0.3050(5)		0.065	0	−0.3050(5)	
O(55)	8*j*	0.065	0.167	−0.3050(5)		0.065	0.167	−0.3050(5)	
O(56)	8*j*	0.065	0.333	−0.3050(5)		0.065	0.333	−0.3050(5)	
O(61)	8*j*	0.633	0.083	−0.3606(5)		0.633	0.083	−0.3606(5)	
O(62)	8*j*	0.633	0.250	−0.3606(5)		0.633	0.250	−0.3606(5)	
O(63)	8*j*	0.633	0.417	−0.3606(5)		0.633	0.417	−0.3606(5)	
O(65)	4*i*	0.383	0	−0.3606(5)		0.383	0	−0.3606(5)	
O(65)	8*j*	0.383	0.167	−0.3606(5)		0.383	0.167	−0.3606(5)	
O(66)	8*j*	0.383	0.333	−0.3606(5)		0.383	0.333	−0.3606(5)	
O(67)	4*i*	0.383	$\frac{1}{2}$	−0.3606(5)		0.383	$\frac{1}{2}$	−0.3606(5)	
O(71)	4*i*	0.028	0	−0.4158(5)		0.028	0	−0.4154(5)	
O(73)	8*j*	0.028	0.333	−0.4158(5)		0.028	0.333	−0.4154(5)	

TABLE 5—*Continued*

		Refinement A				Refinement B			
Atom	Site	x	y	z	Fe occupancy	x	y	z	Fe occupancy
O(74)	8*j*	0.028	$\frac{1}{2}$	−0.4158(5)		0.028	$\frac{1}{2}$	−0.4154(5)	
O(75)	4*i*	0.278	0.083	−0.4158(5)		0.278	0.083	−0.4154(5)	
O(76)	8*j*	0.278	0.250	−0.4158(5)		0.278	0.250	−0.4154(5)	
O(77)	8*j*	0.278	0.417	−0.4158(5)		0.278	0.417	−0.4154(5)	
O(81)	8*j*	0.093	0.083	−0.4722(6)		0.093	0.083	−0.4723(5)	
O(82)	8*j*	0.093	0.250	−0.4722(6)		0.093	0.250	−0.4723(5)	
O(83)	8*j*	0.093	0.417	−0.4722(6)		0.093	0.417	−0.4723(5)	
O(84)	4*i*	0.343	0	−0.4722(6)		0.343	0	−0.4723(5)	
O(86)	8*j*	0.343	0.333	−0.4722(6)		0.343	0.333	−0.4723(5)	
M(0.1)	2*a*	0	0	0	0.22	0	0	0	0.22
M(0.2)	4*g*	0	0.340(3)	0	0.22	0	0.343(3)	0	0.22
M(11)	8*j*	0.147(6)	0.170(3)	−0.0494(5)	0.22	0.151(6)	0.171(3)	−0.0485(5)	0.22
M(12)	4*i*	0.146(8)	$\frac{1}{2}$	−0.0534(10)	0.22	0.145(8)	$\frac{1}{2}$	−0.0531(9)	0.22
M(21)	8*j*	0.124(6)	0.168(3)	−0.1154(4)	0.22	0.125(6)	0.166(3)	−0.1150(4)	0.22
M(22)	4*i*	0.133(8)	$\frac{1}{2}$	−0.1062(8)	0.22	0.127(8)	$\frac{1}{2}$	−0.1064(8)	0.22
M(31)	8*j*	0.442(6)	0.166(3)	−0.1635(5)	0.22	0.444(6)	0.167(3)	−0.1634(5)	0.22
M(32)	4*i*	0.455(7)	$\frac{1}{2}$	−0.1674(9)	0.22	0.453(6)	$\frac{1}{2}$	−0.1670(9)	0.22
M(41)	4*i*	0.265(8)	0	−0.2118(10)	0.22	0.263(8)	0	−0.2126(10)	0.22
M(42)	8*j*	0.255(5)	0.334(3)	−0.2144(5)	0.22	0.256(5)	0.333(3)	−0.2143(5)	0.22
M(51)	4*i*	0.236(8)	0	−0.2787(9)	0.22	0.237(7)	0	−0.2778(9)	0.22
M(52)	8*j*	0.217(4)	0.335(3)	−0.2848(5)	0.22	0.225(4)	0.334(3)	−0.2848(4)	0.22
M(53)	8*j*	0.082(5)	0.162(2)	−0.2654(3)	1.00	0.077(5)	0.165(2)	−0.2652(3)	1.00
M(60)	8*j*	0.476(4)	0.239(2)	−0.3292(7)	0.22	0.481(4)	0.246(2)	−0.3311(7)	0.22
M(61)	8*j*	0.473(4)	0.431(2)	−0.3316(8)	0.22	0.474(4)	0.426(2)	−0.3323(8)	0.22
M(63)	8*j*	0.227(4)	0.162(2)	−0.3363(8)	0.22	0.250(4)	0.160(2)	−0.3337(10)	0.22
M(76)	4*i*	0.205(8)	0	−0.3778(8)	0.22	0.198(7)	0	−0.3766(8)	0.22
M(77)	8*j*	0.215(5)	0.324(2)	−0.3847(5)	0.22	0.208(6)	0.321(2)	−0.3843(4)	0.22
M(78)	4*i*	0.213(0)	$\frac{1}{2}$	−0.3872(0)	0.22	0.213(0)	$\frac{1}{2}$	−0.3872(0)	0.22
M(79)	8*j*	0.443(4)	0.104(2)	−0.3967(6)	0.22	0.443(4)	0.102(2)	−0.3972(6)	0.22
M(81)	4*i*	0.183(8)	0	−0.4512(10)	0.22	0.182(7)	0	−0.4505(10)	0.22
M(82)	8*j*	0.181(6)	0.334(3)	−0.4466(6)	0.22	0.182(6)	0.332(3)	−0.4466(6)	0.22
M(84)	4*i*	0	$\frac{1}{2}$	−0.4598(6)	1.00	0	$\frac{1}{2}$	−0.4605(6)	1.00
M(91)	4*h*	0	0.172(3)	$-\frac{1}{2}$	0.22	0	0.172(3)	$-\frac{1}{2}$	0.22

Note. Biso thermal factors for Ba^{2+}, [Fe^{3+}, Ti^{4+}] and O^{2-} are 0.66(1), 0.61(4) and 0.87(5), respectively. Due to the huge correlation of occupancy factors with others parameters, a common (Fe/Ti) occupancy factor is used for M atoms. Atom identification is as follows: the first number is the layer number and the second number is the atom number within the layer.

and 2.31% for the c-$Ba(Ti,Fe)O_3$ phase. The phase mass fractions were nearly the same as previously 45.01%, 25.56% and 29.43% and corresponded to nearly the same sample composition: $Ba_{42}Ti_{46.0}Fe_{27.8}O_{176.7}$. The cell parameters were fixed at the values obtained in the last refinement for the three phases and the profile parameters were independently refined for each phase (Table 1). The final atomic positions of the J-phase for this refinement B are reported in the second column of Table 5. The atomic positions of the refined Grey phase are reported in the second column of Table 4 and compared with those published in Ref. (5) (first column).

An additional refinement was performed, assuming that the cationic compositional parameters of this $Ba_{12}Ti_{15}Fe_{28}O_{84}$ phase could also slightly change. Subsequent refinements of the J-phase give rise to nearly the same positions with only slightly different overall Fe/Ti occupancies. However, no significant improvement was obtained regarding the agreement factors. The unweighted and weighted profile factors are 9.82% & 13.20%, and the Bragg R factors for the J-phase, the Grey phase and the c-$Ba(Ti,Fe)O_3$ phase are 5.62%, 7.76% and 2.36%, respectively. It is concluded that there is not enough sensitivity to go so far in the Fe/Ti refinements.

Additional refinements were also performed, assuming a total or a partial positional disorder of the pseudo-"$Ba_{12}Ti_{15}Fe_{28}O_{84}$" or H structural blocks (with a $b/3$ or a $2b/3$ translation along the b-axis), their structure remaining uniform within each slab. This type of disorder

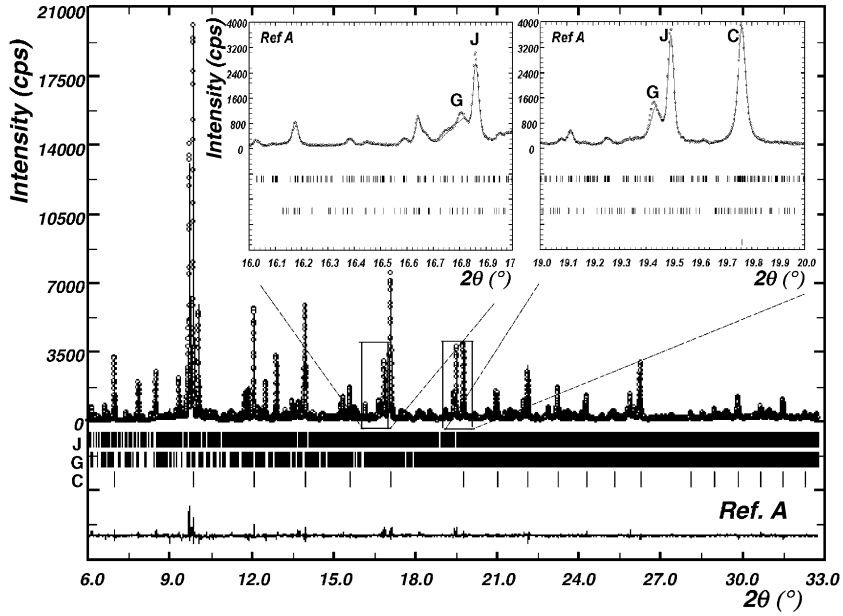

FIG. 3. Observed (dots), calculated (line), difference (bottom) and Bragg reflections (|) of the D2AM-ESRF full diffraction pattern corresponding to the Rietveld refinement A. The inserts enlarge 2Θ area presenting strong reflections of the Grey phase occurring at high 2Θ angle (a) 16–17° and (b) 19–20°.

kills or decreases the intensity of the weak reflections related to the triple *b*-axis and gives rise to nearly the same agreement factor for total disorder (unweighted and weighted profile factors: 10.40% and 13.90%, Bragg *R* factor for the J-phase, the Grey phase and the c-$Ba(Ti,Fe)O_3$ phase: 6.14%, 8.60% and 2.31%, respectively). A small improvement is obtained for partial disorder with domains corresponding to ratios 8/10, 1/10 and 1/10 (unweighted and weighted profile factors: 9.85% amd 13.10% , Bragg *R* factor for the J-phase, the Grey phase and the c-$Ba(Ti,Fe)O_3$ phase: 5.85%, 7.84% and 2.26%, respectively). However, given the larger degree of freedom, the improvement obtained by using these models is not significant and we consider that our data do not contain enough sensitivity to take into account such disorder. Nevertheless, without any initial assumption, the structure assumed to remain uniform within each H slab of the J-phase (layers 5, 6, 7 and 8), which contains a low symmetry and a large *b*-axis very close to what is observed for the $Ba_{12}Ti_{15}Fe_{28}O_{84}$ compound (5). This latter phase coexists in the same batch for the present thermal treatment conditions and its presence also supports the large *b*-axis used for the J-phase. Finally, we assume that the refinement B is the most relevant. This refinement uses a charge-equilibrated composition for the J-phase: $Ba_{42}Ti_{51}Fe_{20}O_{174}$ without any oxygen vacancy. The final corresponding atomic parameters are reported in the second column of Table 5 and a few selected interatomic distances are shown in Table 6.

RESULTS AND DISCUSSION

The Rietveld analysis presented herein is not a full structural refinement of all the atomic parameters independently, since we have restricted displacements of the oxygen parameters and the Ti/Fe occupancies. Thus, this analysis can also be considered as a structural simulation, and the mathematical standard deviations of the *xyz* parameters are underestimated. All the parameter restrictions are required because of the huge reflections overlapping generated by the large cell parameters of the J-phase and the presence of two additional phases. Nevertheless, our intensity analysis nicely fits the experimental pattern and, excepting the too short M12-M22 distance (possibly related to a partial site disorder), gives rise to reasonable interatomic distances. The corresponding structure of the J-phase can be compared and discussed with the previous structural models based on electron microscopy data (9). The J structure crystallizes in the *C2/m* space group with the lattice parameters reported in Table 1 and adopts a close-packed structure built from either ccp or hcp (Ba,O) layers, stacked along the *c*-axis in an 18-layer (chcchhhhcchhhhcchc) sequence. It can be described in a rhombohedral space symmetry with a $c_{rh}-\text{axis} = 127.19\,\text{Å}$ corresponding to the stacking of 54-layers $(chcchhhhcchhhhcchc)_3$ as shown in Fig. 2. This cp stacking is slightly different from the 3×18 stacking $(chcchchcccchchcchc)_3$ proposed by Bendersky *et al.* (9). The observed cell parameters give values $a_{monocl}/\sqrt{3} =$

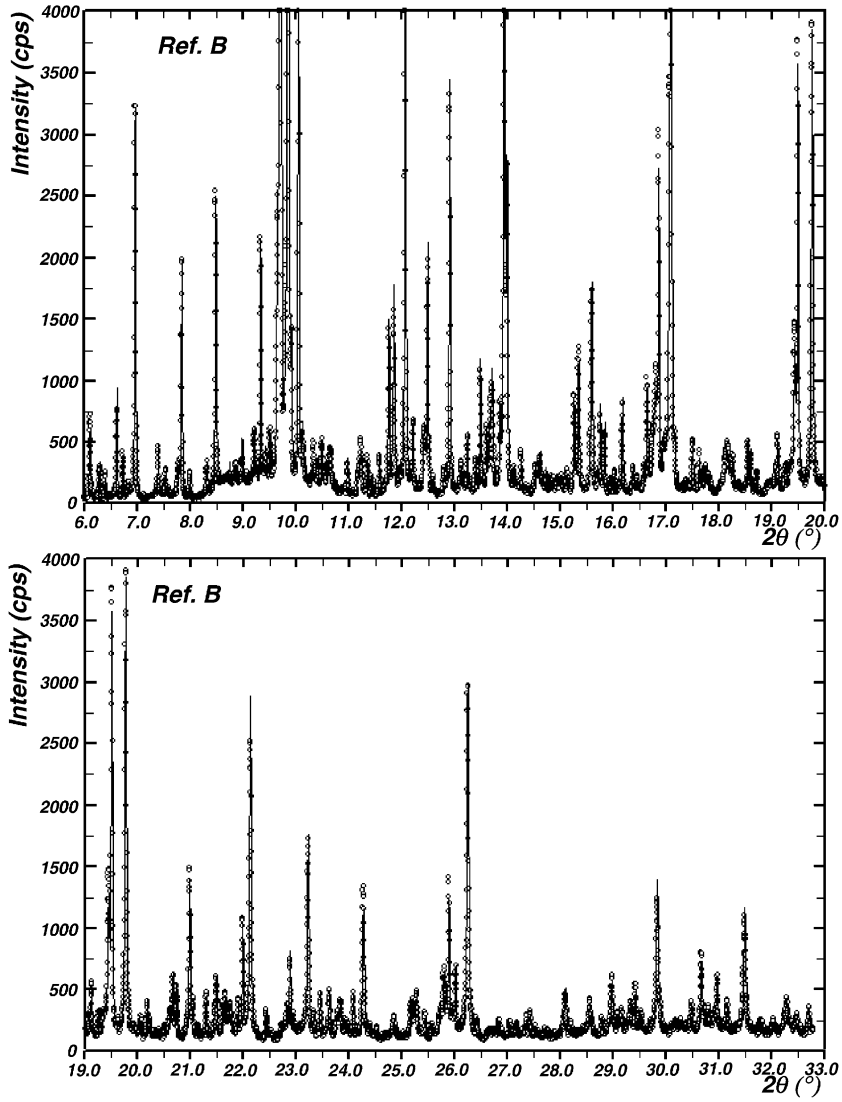

FIG. 4. Enlargements of the Rietveld analysis for the refinement B of the D2AM-ESRF diffraction pattern: (a) $2\Theta = 6$–20° and (b) $2\Theta = 19$–33°; observed (dots), calculated (line).

5.7453 Å very close to $b_{\text{monocl}}/3 = 5.7455$ Å and correspond to a nearly perfect hexagonal lattice with $a_{\text{hexag}} = 5.745$ Å. As first proposed by Bendersky *et al.* (9), this 54-layer stacking can be related to the $(\text{chc})_2$ of the hexagonal 6 H phase and the $(\text{chcccchc})_3$ of the $Ba_{12}Ti_{15}Fe_{28}O_{84}$ phase.

The description of the 18 different (Ba,O) layers, with their octahedral and tetrahedral sites, is given in Fig. 5. These layers are close to those of both the h-$Ba(Ti,Fe)O_3$ phase and the Grey phase (5, 6). Layers 0, 1, 2, 3 and 4 correspond to the hexagonal $Ba(Ti,Fe)O_3$ stacking which is the P block proposed by Bendersky. Layers 5, 6, 7, 8 and 9 are very close to the H block of the same description; they are also close to the stacking found in the $Ba_{12}Ti_{15}Fe_{28}O_{84}$ phase (5). However, we observe a difference in the connecting plane between the P and H blocks. As reported in layer 5, opposed to what was found in the zero layer of the Grey phase [Fig. 1a in Ref. (5)], only a single tetrahedral site exists since the second tetrahedron suggested by the H block description (9) would overlap the octahedral sites of the P block. In the $Ba_{12}Ti_{15}Fe_{28}O_{84}$ phase refined by Grey *et al.* (5), the position of this second tetrahedral site is driven by the presence of a mirror symmetry plane. Furthermore, relative to the stacking of the Grey phase (and the Bendersky *et al.* model), we found an inversion in the orientation of the triangular cluster formed by edge-sharing octahedra in layers 6 and 7. This inversion corresponds to a different cp stacking and reveals the weak probability to have face-sharing octahedra in Ba–

TABLE 6
Interatomic Distances of the J Phase: $Ba_{42}Ti_{51}Fe_{20}O_{174}$ Corresponding to Refinement B

***M*(01) polyhedron**	***M*(60) octahedron**	Ba(04) O(07) 3.14(3)	**Ba(34) polyhedron**	**Shortest M–M distances**
M(01) O(01) 2.06(1) (× 4)	*M*(60) O(52) 2.06(4)	Ba(04) O(11) 2.60(3)	Ba(34) O(23) 2.83(2) (× 2)	*M*(11) *M*(21) 2.82(3)
M(01) O(07) 2.06(1) (× 2)	*M*(60) O(55) 2.01(4)	Ba(04) O(15) 2.53(2) (× 2)	Ba(34) O(27) 2.89(3)	*M*(12) *M*(22) 2.26(5)
***M*(02) polyhedron**	*M*(60) O(56) 1.92(4)	**Ba(06) polyhedron**	Ba(34) O(33) 2.87(1) (× 2)	
M(02) O(02) 2.18(4) (× 2)	*M*(60) O(62) 2.04(4)	Ba(06) O(01) 2.87(2)	Ba(34) O(35) 2.82(2) (× 2)	*M*(41) *M*(51) 2.77(6)
M(02) O(03) 1.95(3) (× 2)	*M*(60) O(65) 2.05(4)	Ba(06) O(01) 3.03(2)	Ba(34) O(37) 2.92(2) (× 2)	*M*(42) *M*(52) 2.99(3)
M(02) O(05) 2.06(1) (× 2)	*M*(60) O(66) 2.14(4)	Ba(06) O(02) 2.88(2)	Ba(34) O(41) 2.82(3)	*M*(51) *M*(53) 3.32(5) (× 2)
***M*(11) polyhedron**	***M*(61) octahedron**	Ba(06) O(02) 2.82(2)	Ba(34) O(47) 2.88(2) (× 2)	*M*(52) *M*(53) 3.41(6)
M(11) O(01) 1.92(4)	*M*(61) O(53) 2.04(4)	Ba(06) O(02) 2.98(2)	**Ba(42) polyhedron**	*M*(52) *M*(60) 3.31(5)
M(11) O(02) 1.80(5)	*M*(61) O(54) 1.90(4)	Ba(06) O(03) 2.92(2)	Ba(42) O(33) 2.93(2)	*M*(53) *M*(60) 3.27(4)
M(11) O(05) 1.85(5)	*M*(61) O(55) 2.13(4)	Ba(06) O(05) 2.83(2)	Ba(42) O(35) 2.96(2)	*M*(53) *M*(61) 3.34(4)
M(11) O(13) 2.16(5)	*M*(61) O(63) 2.07(4)	Ba(06) O(05) 3.04(2)	Ba(42) O(36) 2.97(2)	*M*(53) *M*(63) 3.50(5)
M(11) O(15) 2.20(4)	*M*(61) O(66) 2.16(4)	Ba(06) O(07) 2.92(2)	Ba(42) O(41) 2.86(2)	
M(11) O(16) 2.09(4)	M(61) O(67) 1.93(4)	Ba(06) O(13) 2.67(2)	Ba(42) O(43) 2.88(2)	*M*(60) *M*(61) 3.10(5)
***M*(12) polyhedron**	***M*(63) polyhedron**	Ba(06) O(16) 2.69(2)	Ba(42) O(45) 2.90(2)	*M*(60) *M*(63) 2.73(5)
M(12) O(03) 1.93(4) (× 2)	*M*(63) O(51) 1.88(4)	Ba(06) O(17) 2.74(2)	Ba(42) O(46) 2.91(2)	*M*(60) *M*(63) 3.14(5)
M(12) O(07) 1.99(7)	*M*(63) O(52) 2.05(4)	**Ba(12) polyhedron**	Ba(42) O(46) 2.85(2)	*M*(61) *M*(61) 2.55(5)
M(12) O(11) 2.00(7)	*M*(63) O(55) 2.29(4)	Ba(12) O(02) 2.85(2)	Ba(42) O(47) 2.84(2)	*M*(61) *M*(63) 3.13(5)
M(12) O(17) 2.05(4) (× 2)	*M*(63) O(62) 2.21(4)	Ba(12) O(03) 2.84(2)	Ba(42) O(51) 2.85(2)	*M*(61) *M*(76) 3.29(7)
***M*(21) polyhedron**	*M*(63) O(63) 2.05(4)	Ba(12) O(05) 2.83(2)	Ba(42) O(52) 2.85(2)	*M*(63) *M*(76) 3.32(4)
M(21) O(13) 2.19(5)	*M*(63) O(65) 1.82(4)	Ba(12) O(11) 2.86(1)	Ba(42) O(56) 2.82(2)	
M(21) O(15) 2.21(4)	***M*(76) polyhedron**	Ba(12) O(13) 2.89(1)	**Ba(44) polyhedron**	*M*(76) *M*(79) 3.19(7) (× 2)
M(21) O(16) 2.21(4)	*M*(76) O(63) 1.73(3) (× 2)	Ba(12) O(15) 2.86(2)	Ba(44) O(31) 3.00(2)	*M*(76) *M*(81) 3.13(5)
M(21) O(21) 1.96(4)	*M*(76) O(64) 1.91(7)	Ba(12) O(16) 2.87(2)	Ba(44) O(37) 2.84(2) (× 2)	*M*(77) *M*(78) 3.08(6)
M(21) O(22) 1.97(4)	*M*(76) O(71) 2.27(6)	Ba(12) O(16) 2.89(2)	Ba(44) O(43) 2.88(2) (× 2)	*M*(77) *M*(79) 2.96(6)
M(21) O(25) 2.01(5)	*M*(76) O(75) 2.37(4) (× 2)	Ba(12) O(17) 2.87(2)	Ba(44) O(45) 3.05(2) (× 2)	*M*(77) *M*(82) 2.65(3)
***M*(22) polyhedron**	***M*(77) polyhedron**	Ba(12) O(22) 2.95(2)	Ba(44) O(47) 2.70(2) (× 2)	*M*(78) *M*(79) 3.22(4) (× 2)
M(22) O(11) 1.95(7)	*M*(77) O(61) 2.10(4)	Ba(12) O(23) 2.94(2)	Ba(44) O(53) 2.85(2) (× 2)	*M*(79) *M*(82) 3.49(6)
M(22) O(17) 2.00(4) (× 2)	*M*(77) O(62) 1.79(4)	Ba(12) O(25) 2.93(2)	Ba(44) O(54) 3.02(2)	*M*(79) *M*(84) 3.30(3)
M(22) O(23) 2.18(4) (× 2)	*M*(77) O(66) 1.95(5)	**Ba(14) polyhedron**	**Ba(57) polyhedron**	
M(22) O(27) 2.24(6)	*M*(77) O(73) 2.15(5)	Ba(14) O(01) 2.82(2) (× 2)	Ba(57) O(41) 3.09(2)	*M*(81) *M*(84) 3.23(7)
***M*(31) polyhedron**	*M*(77) O(76) 1.97(4)	Ba(14) O(07) 2.80(3)	Ba(57) O(47) 3.27(2) (× 2)	*M*(82) *M*(84) 3.44(5)
M(31) O(22) 1.93(4)	*M*(77) O(77) 2.25(3)	Ba(14) O(13) 2.87(1) (× 2)	Ba(57) O(51) 2.71(2) (× 2)	*M*(84) *M*(84) 3.36(3)
M(31) O(23) 1.93(4)	***M*(78) polyhedron**	Ba(14) O(15) 2.88(2) (× 2)	Ba(57) O(53) 3.10(2) (× 2)	
M(31) O(25) 1.90(5)	*M*(78) O(61) 2.03(1) (× 2)	Ba(14) O(17) 2.86(2) (× 2)	Ba(57) O(56) 2.91(4) (× 2)	
M(31) O(33) 2.09(5)	*M*(78) O(67) 1.96(1)	Ba(14) O(21) 2.97(2) (× 2)	Ba(57) O(61) 2.66(2) (× 2)	
M(31) O(35) 2.08(4)	*M*(78) O(74) 2.12(1)	Ba(14) O(27) 2.95(3)	Ba(57) O(64) 2.40(2)	
M(31) O(36) 2.07(4)	*M*(78) O(77) 2.01(1) (× 2)	**Ba(24) polyhedron**	**Ba(72) polyhedron**	
***M*(32) polyhedron**	***M*(79) polyhedron**	Ba(24) O(11) 2.83(3)	Ba(72) O(62) 2.80(2)	
M(32) O(21) 1.97(3) (× 2)	*M*(79) O(61) 2.38(4)	Ba(24) O(15) 2.75(2) (× 2)	Ba(72) O(63) 2.84(2)	
M(32) O(27) 2.07(6)	*M*(79) O(64) 2.46(3)	Ba(24) O(21) 2.80(2) (× 2)	Ba(72) O(66) 2.80(2)	
M(32) O(31) 1.91(6)	*M*(79) O(65) 2.04(3)	Ba(24) O(23) 2.98(2) (× 2)	Ba(72) O(71) 2.91(2)	
M(32) O(37) 2.03(4) (× 2)	*M*(79) O(73) 1.63(3)	Ba(24) O(25) 2.89(3) (× 2)	Ba(72) O(73) 2.84(2)	
***M*(41) polyhedron**	*M*(79) O(74) 2.13(3)	Ba(24) O(31) 2.98(3)	Ba(72) O(75) 2.88(2)	
M(41) O(31) 1.86(7)	*M*(79) O(75) 1.79(4)	Ba(24) O(35) 3.05(2) (× 2)	Ba(72) O(76) 2.85(2)	
M(41) O(35) 1.85(4) (× 2)	***M*(81) polyhedron**	**Ba(26) polyhedron**	Ba(72) O(76) 2.86(2)	
M(41) O(41) 2.29(6)	*M*(81) O(71) 2.22(6)	Ba(26) O(13) 2.71(2)	Ba(72) O(77) 2.91(2)	
M(41) O(45) 2.30(4) (× 2)	*M*(81) O(75) 2.23(4) (× 2)	Ba(26) O(16) 2.67(2)	Ba(72) O(81) 2.99(2)	
***M*(42) polyhedron**	*M*(81) O(81) 1.89(4) (× 2)	Ba(26) O(17) 2.75(2)	Ba(72) O(82) 2.95(2)	
M(42) O(33) 1.84(5)	*M*(81) O(84) 1.91(7)	Ba(26) O(21) 2.95(2)	Ba(72) O(86) 2.97(2)	
M(42) O(36) 1.91(4)	***M*(82) polyhedron**	Ba(26) O(22) 2.85(2)	**Ba(85) polyhedron**	
M(42) O(37) 1.91(4)	*M*(82) O(73) 2.11(5)	Ba(26) O(22) 2.87(2)	Ba(85) O(73) 2.86(2)	
M(42) O(43) 2.29(4)	*M*(82) O(76) 2.12(4)	Ba(26) O(23) 2.93(2)	Ba(85) O(75) 2.88(2)	
M(42) O(46) 2.23(4)	*M*(82) O(77) 2.14(4)	Ba(26) O(25) 2.82(2)	Ba(85) O(76) 2.93 (2)	
M(42) O(47) 2.23(4)	*M*(82) O(82) 1.96(4)	Ba(26) O(27) 2.97(2)	Ba(85) O(81) 2.89(2)	
***M*(51) polyhedron**	*M*(82) O(83) 1.99(4)	Ba(26) O(33) 3.09(2)	Ba(85) O(82) 2.94(2)	
M(51) O(41) 2.06(6)	*M*(82) O(86) 2.00(5)	Ba(26) O(36) 3.06(2)	Ba(85) O(82) 2.86(2)	
M(51) O(45) 2.02(4) (× 2)	***M*(84) tetrahedron**	Ba(26) O(37) 3.13(2)	Ba(85) O(82) 2.93(2)	
M(51) O(51) 2.03(4) (× 2)	*M*(84) O(74) 1.92(3)	**Ba(32) polyhedron**	Ba(85) O(83) 2.81(2)	
M(51) O(54) 1.99(6)	*M*(84) O(83) 1.80(1) (× 2)	Ba(32) O(21) 2.72(2)	Ba(85) O(83) 2.87(2)	

TABLE 6—*Continued*

***M*(52) polyhedron**	*M*(84) O(84) 1.61(1)	Ba(32) O(22) 2.75(2)	Ba(85) O(84) 2.82(2)
M(52) O(43) 2.32(4)	***M*(91) polyhedron**	Ba(32) O(25) 2.81(2)	Ba(85) O(86) 2.93(2)
M(52) O(46) 2.18(4)	*M*(91) O(81) 2.10(4) (× 2)	Ba(32) O(31) 2.84(2)	Ba(85) O(86) 2.94(2)
M(52) O(47) 2.16(4)	*M*(91) O(82) 1.97(4) (× 2)	Ba(32) O(33) 2.91(2)	**Ba(87) polyhedron**
M(52) O(52) 1.94(4)	*M*(91) O(86) 2.03(1) (× 2)	Ba(32) O(35) 2.92(2)	Ba(87) O(71) 2.80(3)
M(52) O(53) 1.92(4)		Ba(32) O(36) 2.95(2)	Ba(87) O(77) 2.78(2) (× 2)
M(52) O(56) 1.75(4)	**Ba(04) polyhedron**	Ba(32) O(36) 2.83(2)	Ba(87) O(81) 2.90(2)
***M*(53) tetrahedron**	Ba(04) O(01) 2.81(2) (× 2)	Ba(32) O(37) 2.79(2)	Ba(87) O(81) 3.03(2) (× 2)
M(53) O(43) 1.77(4)	Ba(04) O(03) 2.96(2)	Ba(32) O(43) 2.91(2)	Ba(87) O(81) 2.90(2) (× 2)
M(53) O(45) 1.76(4)	Ba(04) O(03) 3.20(2) (× 2)	Ba(32) O(45) 2.96(2)	Ba(87) O(83) 2.86(2) (× 2)
M(53) O(46) 1.81(4)	Ba(04) O(03) 2.96(2)	Ba(32) O(46) 2.99(2)	Ba(87) O(84) 3.01(3)
M(53) O(55) 1.69(2)	Ba(04) O(05) 2.89(2) (× 2)		Ba(87) O(86) 2.88(2) (× 2)

Ti–Fe–O structures. As an example, in $Ba_6Ti_{17}Fe_{45}O_{106}$ (21) there was no face sharing between the octahedra, and in hexagonal h-$BaTiO_3$ face-sharing occurs only every three layers to avoid the presence of two shared faces in any octahedron. In the refined J-phase, nearly all octahedra are linked to each other by edges and vertices, there are only a few face-sharing connections in the P blocks and the stacking inversion observed in layer 6 favors edge-sharing connections at the interface of P and H blocks. Without this inversion there would be an additional face-sharing and the formation of a row of three successive face-sharing octahedra which would give rise to octahedral sites with two shared faces. On the other hand, tetrahedral sites are localized either at the P/H block interface or at the middle of the H block. The middle of the H block corresponds to a small cubic perovskite stacking along its three-fold axis.

All Ba cations are 12-coordinated and, in the monoclinic $C2/m$ cell, 12 Fe cations are surrounded by an oxygen tetrahedron, and 130 octahedra are occupied by Ti or Fe cations. The resulting formulae is $^{XII}Ba^{VI}_{42}(Ti_xFe_{1-x})^{IV}_{65}Fe_6O_{174}$. Cations–oxygen distances are reported in Table 6 and correspond to the most significant refinement B (second column of Tables 2–5) performed without oxygen vacancies with an overall Ti/Fe occupancy factor that gives a charge equilibrated formulae $^{XII}Ba^{VI}_{42}(Ti_{51}Fe_{14})^{IV}Fe_6O_{174}$. We observe a difference between this oxidized composition $Ba_{42}Ti_{51}Fe_{20}O_{174}$ and the two "model" compositions $Ba_{42}Ti_{45}Fe_{28}O_{174}/Ba_{42}Ti_{46}Fe_{28}O_{176}$ proposed by Bendersky *et al.* (9) and the single crystal composition $Ba_{36}Ti_{48}Fe_{24}O_{168}$ ($Ba_3Ti_4Fe_2O_{14}$) proposed by Vanderah *et al.* (3) We must remind that (i) single crystals can be extracted from a batch having a slightly different overall composition, (ii) oxygen vacancies can be associated in this system with a smaller Ti^{4+}/Fe^{3+} ratio or with some cation vacancies (although X rays are mainly sensitive to cations). The oxygen vacancies in the (Ba,O) layers are possible in layers 1 and 4 corresponding to the pseudo h-$Ba(Ti,Fe)O_3$ blocks containing a Ba zigzag arrangement (Figs. 2 and 6), as it was found in the corresponding hexagonal h-Ba $(Ti_{1-x}Fe_x)O_{3-\delta}$ structure. Grey *et al.* (6) have shown in this latter phase that, for high Fe substitution, oxygen vacancies are only present in the (Ba,O) layer of the plane corresponding to the change of direction of the Ba row, this plane contains the only oxygen face-shared octahedron. The maximum oxygen vacancy content in this phase is $x \cong \frac{2}{3}$ corresponding to a ($BaO_{2.00}$) layer giving rise to the overall formulae $BaFeO_{2.66}$. Such vacancies are observed after classical thermal treatment under air. As for our preparation of the J-phase we also have annealed under air at high temperature, it is probable that there are also a few oxygen vacancies in the h-$Ba(Ti,Fe)O_3$-like structural P block. With this hypothesis, the maximum number of O-vacancies would exist for the maximum Fe substitution in the Ti/Fe octahedral sites of the P block. They would occur in (Ba,O) planes labeled O1i and O4i; with a Ti^{4+}/Fe^{3+} ratio corresponding to a charge equilibrated formulae, they would give rise to the $^{XII}Ba^{VI}_{42}(Ti_{27}Fe_{38})^{IV}Fe_6O_{162}$ composition.

For every refinements, the significant (Ba,O) stacking along the *c*-axis in the unit cell is

$$Ba_6O_{18}/Ba_6O_{18}/Ba_6O_{18}/Ba_6O_{18}/Ba_6O_{18}/Ba_2O_{22}$$
$$/O_{24}/Ba_4O_{20}/Ba_6O_{18}/Ba_6O_{18}/Ba_4O_{20}/O_{24}/Ba_2O_{22}$$
$$/Ba_6O_{18}/Ba_6O_{18}/Ba_6O_{18}/Ba_6O_{18}/Ba_6O_{18}.$$

Based on refinement B, the Ti/Fe distribution along the *c*-axis is

$$Ti_{4.7}Fe_{1.3}/Ti_{4.7}Fe_{1.3}/Ti_{4.7}Fe_{1.3}/Ti_{4.7}Fe_{1.3}/Ti_{4.7}Fe_{1.3}$$
$$/Ti_{4.7}Fe_{5.3}/Ti_{9.4}Fe_{2.6}/Ti_{9.4}Fe_{2.6}/Ti_{4.7}Fe_{3.3}/Ti_{3.2}Fe_{0.8}$$
$$/Ti_{4.7}Fe_{3.3}/Ti_{9.4}Fe_{2.6}/Ti_{9.4}Fe_{2.6}/Ti_{4.7}Fe_{5.3}/Ti_{4.7}Fe_{1.3}$$
$$/Ti_{4.7}Fe_{1.3}/Ti_{4.7}Fe_{1.3}/Ti_{4.7}Fe_{1.3}.$$

and presents no important Fe/Ti modulation along the *c*-axis contrary to previously reported zero-loss filtered high-resolution images (7). However, further analyses are needed to determine the Ti/Fe occupancies, in particular additional diffraction experiments on closely related samples with slightly different compositions and/or chemically sensitive experiments like the neutron or X-ray

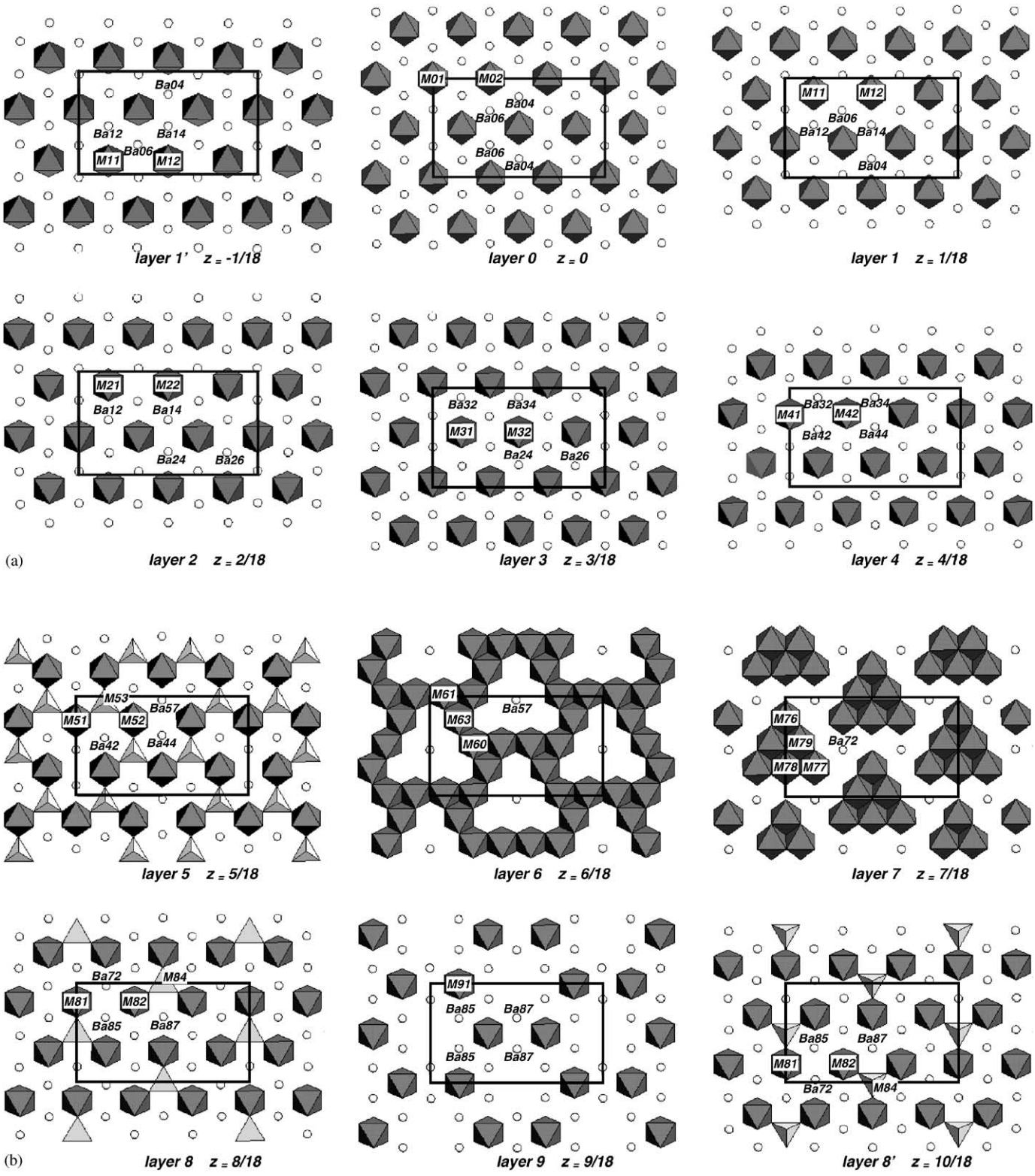

FIG. 5. Successive (*a b*) layers existing in J-phase 1′-layer, 0-layer, 1-layer, 2-layer, 3-layer, 4-layer, 5-layer, 6-layer, 7-layer, 8-layer, 9-layer, 8'-layer, … .

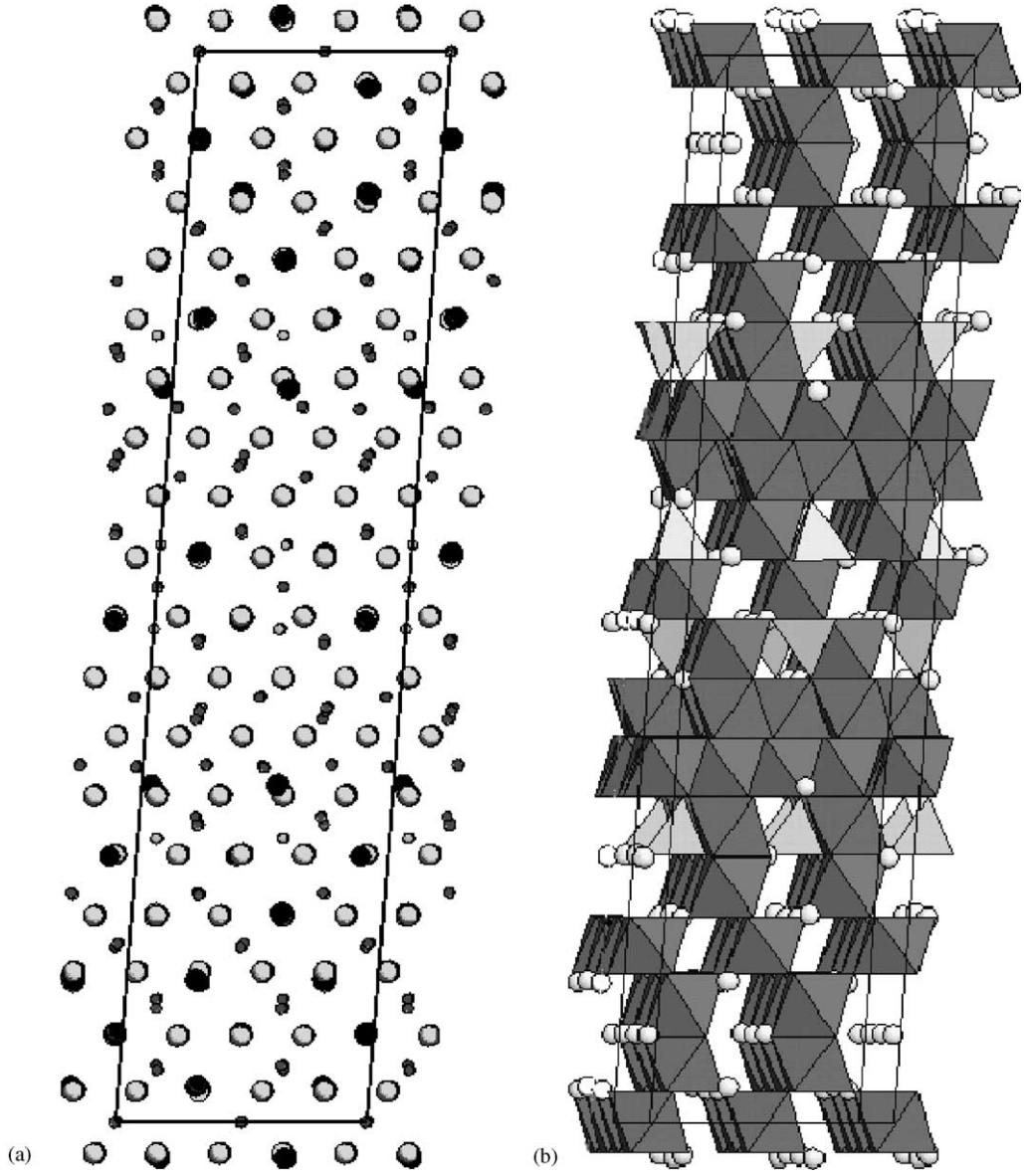

FIG. 6. (a) Stacking along the *c*-axis of O (large open spheres) Ba (large full spheres) and Ti/Fe (small spheres) atoms occurring in the J-phase and (b) polyhedra stacking of the J-phase represented with nearly the same projection, octahedral sites are darker than the tetrahedral ones.

anomalous scattering measurements. In conclusion, this structure refinement/simulation supports the existence of a new "native multilayered" series as proposed by Bendersky *et al*. (9). However, it is not obvious that these compounds present a strong Ti/Fe periodicity as it occurs in artificial magnetic multilayers.

ACKNOWLEDGMENTS

Financial support from ECOS/SeCyT cooperation project (A97E07) is acknowledged. R. E. C. thanks SeCyT-UNC, Agencia Córdoba Ciencia and ANPCyT for financial support. We also acknowledge I. E. Grey for helpful supports.

REFERENCES

1. G. Geiger, *Am. Ceram. Soc. Bull.* **73,** 57 (1994); T. Abraham, *Am. Ceram. Soc. Bull.* **73,** 62 (1994).
2. R. C. Buchanan (Ed.), "Ceramic Materials for Electronics," Marcel Dekker, New York, 1991.
3. T. A. Vanderah, J. M. Loezos, and R. S. Roth, *J. Solid State Chem.* **121,** 38 (1996).
4. L. A. Bendersky, T. A. Vanderah, and R. S. Roth, *J. Solid State Chem.* **125,** 281 (1996).

5. I. E. Grey, A. Collomb, and X. Obradors, *J. Solid State Chem.* **91,** 131 (1991).
6. I. E. Grey, C. Li, L. M. D. Cranswick, R. S. Roth, and T. A. Vanderah, *J. Solid State Chem.* **135,** 312 (1998).
7. L. A. Bendersky and J. E. Bonevich, *Philos. Mag. Lett.* **77,** 279 (1998).
8. T. Siegrist, C. Svensson, T. A. Vanderah, and R. S. *Roth, Solid State Sci.* **2,** 539 (2000).
9. L. A. Bendersky, T. A. Vanderah, and R. S. Roth, *Philos. Mag. A* **78,** 1299 (1998).
10. A. Fitch, *IUCr Commun. Powder Diff. Newslett*, **17,** 1 (1996).
11. J. L. Hodeau, P. Bordet, M. Anne, A. Prat, A. Fitch, and E. Dooryhee, G. Vaughan, A. Freud, SPIE **3448,** 353 (1998).
12. D. T. Cromer and J.T. Waber, *Acta Crystallogr.* **15,** 104 (1965).
13. S. Sasaki, "Anomalous Scattering Factors for Synchrotron Radiation Users," National Lab. For High Energy Physics, Japan, 1984.
14. D. T. Cromer and D. Liberman, *J. Chem. Phys.* **53,** 1981 (1970).
15. D. T. Cromer and D. Liberman, *Acta Crystallogr. A* **37,** 267 (1981).
16. H. M. Rietveld, *Acta Crystallogr.* **22,** 151 (1967).
17. J. Rodriguez Carvajal, *Physica B* **192,** 55 (1993).
18. R. H. Buttner and E. N. Maslen, *Acta Crystallogr. B* **48,** 764 (1992).
19. L. W. Finger, D. E. Cox, and A. P. Jephcoat, *J. Appl. Crystallogr.* **27,** 892 (1994).
20. R. D. Shannon, *Acta Crystallogr. A* **32,** 751 (1976).
21. T. A. Vanderah, W. Wong-Ng, B. H. Toby, V. M. Browning, R. D. Shull, R. G. Geyer, and R. S. Roth, *J. Solid State Chem.* **143,** 182 (1999).